Linear stability of an alternating-magnetic-field-driven flow in a spinning cylindrical container

Victor Shatrov,[1] Gunter Gerbeth,[1,*] and Regina Hermann[2]
[1]*Forschungszentrum Dresden-Rossendorf, P. O. Box 510119, D-01314 Dresden, Germany*
[2]*Leibniz Institute for Solid State and Materials Research (IFW) Dresden, Helmholtzstrasse 20, D-01069 Dresden, Germany*
(Received 17 January 2008; published 18 April 2008)

We present a numerical analysis of free-surface liquid metal flow and its three-dimensional linear stability. The flow is driven by an alternating magnetic field in a spinning cylindrical container. The electromagnetic and hydrodynamic fields are fully coupled via the shape of the liquid free surface. The hydrodynamic equations are solved by a spectral collocation method, and the alternating magnetic field distribution is found by a boundary-integral method. The flow stability is analyzed for various magnetohydrodynamic interaction parameters and Ekman numbers assuming a flat free surface. We find that only a sufficiently fast spinning suppresses and stabilizes the flow, but a moderate spinning can significantly destabilize it.

DOI: 10.1103/PhysRevE.77.046307 PACS number(s): 47.20.−k, 47.32.Ef, 47.65.−d

I. INTRODUCTION

The rotating flow in a cylindrical container represents a generic problem in fluid mechanics. For instance, the symmetry breaking in a free-surface cylinder flow was analyzed by Lopez *et al.* [1], where the motion was driven by a constant rotation of the bottom wall. This flow is unstable to three-dimensional perturbations for sufficiently large rotation rates [1]. The three-dimensional instability of the axisymmetric flow driven by a rotating lid of a cylindrical enclosure was studied by Gelfgat *et al.* [2].

If the considered fluid is electrically conducting, external magnetic fields provide an interesting tool for a contactless stirring of the melt. Various flow topologies are possible depending on the feeding currents in the coil system that create the external alternating magnetic field. A rotating magnetic field, for instance, drives in a cylindrical container a primarily azimuthal flow which is accompanied by a meridional flow caused by the solid bottom and the upper boundary of the fluid volume [3]. The stability of this flow was analyzed by Grants and Gerbeth [4,5]. The flow stability in the case of a combined action of a rotating magnetic field and a mechanical rotation of the container was investigated by Pedchenko and Grants [6]. A purely meridional base flow is driven by an alternating magnetic field created by a corresponding alternating current in an axisymmetric coil system, which is vertically placed around the cylindrical container. In this case, the magnetic field is basically in the vertical direction and the induced electrical current is an azimuthal one. The interaction of this induced electric current and the magnetic field gives rise to a time-independent Lorentz force distribution which drives a radial-meridional flow. This type of melt stirring is well known for electromagnetic induction heating. The flow field in a cylindrical container placed inside an induction heater has been the subject of several investigations [7–9], addressing mainly the turbulence characteristics of such a confined flow field.

The combination of this electromagnetic meridional flow driving force with a mechanical rotation of the liquid container represents an interesting tool to arrange the flow field inside the liquid. Meridional and azimuthal flow components are fully coupled. For instance, a suppression of the meridional flow can be expected for an increasing spinning rate of the container, whereas the meridional flow driving should also change the azimuthal flow. This superposition of global rotation and electromagnetic flow driving was recently considered for the case of a spherical droplet as typically occurs in electromagnetic levitation processing [10]. The possibility of flow tailoring by the combination of mechanical rotation and electromagnetic stirring has recently received application in solidification studies [11,12]. Filip *et al.* [11] showed that a distinct reduction of the soft magnetic α-Fe phase can be obtained in the solidification of Nd-Fe-B alloys, if the melt crucible undergoes a mechanical rotation during solidification. The configuration used in [11] corresponds almost exactly to the one considered here: a rotating cylindrical crucible is placed in a longer induction coil. Similarly, a strong influence of electromagnetic melt stirring on the morphology was found for solidified Ti-Al alloys [12].

In the present paper we analyze numerically the flow driven by an alternating external magnetic field and an additional global rotation of the liquid container. The axisymmetric base flow for this case has recently been addressed by Shatrov *et al.* [13]. We briefly recall this approach in Sec. II and present some further numerical results. The free liquid surface depends on the flow field and the contact angle to the sidewall. The externally applied magnetic field is strongly modified by the presence of the conducting liquid. Thus, the calculation of the electromagnetic forces is fully coupled to the flow field via the shape of the free surface of the liquid.

The main content of the present paper in Sec. III deals with the linear three-dimensional stability of the considered flow. When the Ekman number, which characterizes the global rotation of the cylindrical container, exceeds a certain value, the free surface is almost flat. In this case the electromagnetic and hydrodynamic equations decouple, which simplifies the flow stability analysis considerably.

II. THE AXISYMMETRIC BASE FLOW

A. Problem formulation

We consider the flow in a cylinder of radius R_0 and height H filled with a liquid metal of electrical conductivity σ, den-

*g.gerbeth@fzd.de

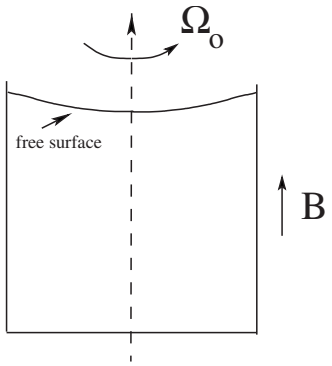

FIG. 1. Sketch of the spinning cylindrical container filled with a free-surface liquid metal.

sity ρ, kinematic viscosity ν, and surface tension γ. The cylinder rotates with angular velocity Ω_0 around its symmetry axis, as shown in Fig. 1. The cylindrical container is placed inside an inductor. The sizes of the inductor are much larger than H, and the alternating magnetic field with frequency ω_0 is approximately uniform and parallel to the container symmetry axis (in the absence of the liquid). The container is made from an electrically insulating material. This alternating magnetic field induces alternating electric currents inside the liquid metal. The interaction of the induced electric currents and the alternating magnetic fields leads to a Lorentz force distribution inside the liquid. The Lorentz force has a stationary component and an oscillating one with double frequency $2\omega_0$. The eddy currents can be used to heat and melt the metal. We consider the thermodynamical equilibrium case; the metal is liquid and an almost uniform temperature distribution is established inside it. For simplicity the temperature is considered as a constant, and all physical properties of the liquid are constant as well. The stationary Lorentz force component drives a meridional flow inside the container. The part of the Lorentz force oscillating with the double frequency is neglected because inertia precludes any noticeable liquid reaction at the considered high frequencies in the range of hundreds of kilohertz. The free surface shape of a liquid depends on the spinning rate, the gravity, the flow in the melt, the liquid surface tension, and the Lorentz force distribution along the surface. The distribution of the magnetic field, in turn, depends on the shape of the free surface. Thus, the flow, the shape of the free surface, the ac magnetic field, and the Lorentz force distribution are fully coupled and must be determined simultaneously.

B. ac magnetic field distribution

In order to calculate the alternating (ac) magnetic field we use the boundary-integral method [14]. Inside the electrically conducting liquid the magnetic field is governed by the induction equation

$$i\omega_0 \boldsymbol{B} = \frac{1}{\mu_0 \sigma} \Delta \boldsymbol{B}, \tag{1}$$

where μ_0 is the permeability of vacuum and σ is the electrical conductivity of the liquid metal. Note that the effect related to the liquid flow (the $\boldsymbol{v} \times \boldsymbol{B}$ term) has been neglected in the equation above, which is a valid approximation for high enough frequencies [15]. Thus, the electromagnetic part of the problem is coupled to the hydrodynamic one only via the free surface shape. For a given free surface we can find the ac magnetic field distribution separately from the hydrodynamic part of the problem. Due to the axisymmetry of the problem, the poloidal magnetic field $\boldsymbol{B}$ under consideration here can be described by using a purely azimuthal vector potential $\boldsymbol{A} = A_\phi \boldsymbol{e}_\phi$ as $\boldsymbol{B} = \nabla \times \boldsymbol{A}$. Hence, the solution of Eq. (1) can be obtained in terms of the scalar $A_\phi(z,r,t)$.

The boundary-integral method [14] is based on the vector potential formulation, and makes use of the Green's functions of Laplace and Helmholtz equations for the exterior and interior regions of the conducting melt. The method reduces the electromagnetic problem to a solution of two coupled boundary-integral equations which are written in cylindrical coordinates,

$$\int_L \left(\frac{\partial \Psi(\boldsymbol{r}')}{\partial n'} r G^0_\phi(\boldsymbol{r},\boldsymbol{r}') - \frac{\Psi(\boldsymbol{r}')}{r'} \frac{\partial r\, r' G^0_\phi(\boldsymbol{r},\boldsymbol{r}')}{\partial n'} \right) d|\boldsymbol{r}'| + 2\pi\Psi(\boldsymbol{r}) = 4\pi\Psi_0(\boldsymbol{r}), \tag{2}$$

$$\int_L \left(\frac{\partial \Psi(\boldsymbol{r}')}{\partial n'} r G^\lambda_\phi(\boldsymbol{r},\boldsymbol{r}') - \frac{\Psi(\boldsymbol{r}')}{r'} \frac{\partial (r r' G^\lambda_\phi(\boldsymbol{r},\boldsymbol{r}'))}{\partial n'} \right) d|\boldsymbol{r}'| - 2\pi\Psi(\boldsymbol{r}) = 0, \tag{3}$$

where $\Psi(\boldsymbol{r}) = rA_\phi(\boldsymbol{r})$. For the assumed uniform external ac magnetic field, $\Psi_0(\boldsymbol{r}) = r^2/2$. The variable $\boldsymbol{r}$ defines a control point on the contour L forming the conducting body of rotation. The Green's functions are [14]

$$G^0_\phi(\boldsymbol{r},\boldsymbol{r}') = \frac{4k}{\sqrt{(r'r)}} \left(\frac{K(k) - E(k)}{k^2} - \frac{K(k)}{2} \right), \tag{4}$$

$$G^\lambda_\phi(\boldsymbol{r},\boldsymbol{r}') = \frac{2k}{\sqrt{(r'r)}} \int_0^{\pi/2} \frac{2\sin^2(\phi) - 1}{\sqrt{[1 - k^2 \sin^2(\phi)]}} \times \exp\{-\kappa\sqrt{[1 - k^2 \sin^2(\phi)]}\} d\phi, \tag{5}$$

where $\kappa = 2\lambda\sqrt{r'r}/k$ and $\lambda^2 = 2i/\delta$ with the dimensionless skin depth $\delta = \sqrt{2/\mu_0 \sigma \omega_0 R_0^2}$. We use also the dimensionless frequency $\omega = \mu_0 \sigma \omega_0 R_0^2$. $K(k)$ and $E(k)$ are the complete elliptic integrals [16] of the first and second kinds, respectively, of the modulus $k = 2\sqrt{r'r/[(r'+r)^2 + (z'-z)^2]}$.

Whereas different techniques for Green's function calculations are described [14], we applied a simple Gauss quadrature directly to the integral (5) using a cubic mapping near the collocation points. Though rather slow, this method gives good accuracy. In order to solve the system (2) and (3) the integration contour L was disctretized by N_{elem} linear elements. Their sizes were reduced near the two corners of the contour using a cubic mapping. This leads to sufficiently small element sizes near the corners of the border, where the solution of the electromagnetic problem has a weak singularity [17,18].

As reported earlier [13], test cases for the magnetic fields in a sphere and a cylinder showed a second-order accuracy of

convergence for this approach. In the present study we shall consider only the case of a fixed frequency of $\omega=2\times10^2$, corresponding to a dimensionless skin depth of $\delta=0.1$. When A_ϕ is found, the time-averaged Lorentz force is obtained in the dimensionless form as $\boldsymbol{f}=\frac{1}{2}\mathrm{Im}(A\boldsymbol{\nabla}A^*)$.

C. Numerical method

We consider the flow inside the cylindrical container in the rotating frame of reference. Scaling length, time, velocity, and pressure by R_0, R_0^2/ν, ν/R_0, and $\rho(\nu/R_0)^2$, respectively, we obtain the following dimensionless governing equations in the rotating frame of reference:

$$\frac{\partial \boldsymbol{v}}{\partial t}+(\boldsymbol{v}\cdot\boldsymbol{\nabla})\boldsymbol{v}+\frac{2}{E}\boldsymbol{e}_z\times\boldsymbol{v}=-\boldsymbol{\nabla}P+\Delta\boldsymbol{v}+N\boldsymbol{f},\quad \boldsymbol{\nabla}\cdot\boldsymbol{v}=0, \tag{6}$$

where $\boldsymbol{f}$ is the Lorentz force given above, $N=\sigma\omega R_0^4B_0^2/(\rho\nu^2)$ is the interaction parameter characterizing the amplitude of the electromagnetic force, and $E=\nu/(\Omega_0R_0^2)$ is the Ekman number. The true thermodynamic pressure p in the fluid is related to the total pressure P by

$$P=p-\frac{r^2}{2E^2}+Gh(r),$$

where G stands for the dimensionless gravity $G=gR_0^3/\nu^2$ with $g=9.87\ \mathrm{m/s^2}$ and $z=h(r)$ denotes the unknown free surface of the fluid.

For the fluid regions in contact with the container walls (the bottom at $z=0$ and the sidewall at $r=1$), the boundary condition for the velocity is the no-slip one $\boldsymbol{v}=\boldsymbol{0}$. On the free surface $z=h(r)$, there is a free-slip condition $e_{ij}t_in_j=0$ and also $v_in_i=0$, where e_{ij} denotes the fluid shear stress and t_i,n_j are the components of the free surface tangential and normal vectors, respectively [19].

For the axysimmetric case, it is convenient to introduce the stream function $\psi(r,z)$; then the meridional velocity components are $v_r=-1/r\ \partial\psi/\partial z$ and $v_z=1/r\ \partial\psi/\partial r$, and the azimuthal component of the vorticity is $w=\partial v_r/\partial z-\partial v_z/\partial r$. In terms of these quantities the Navier-Stokes equations (6) for the steady case are

$$\frac{\partial(v_zw)}{\partial z}+\frac{\partial(v_rw)}{\partial r}-\frac{2v_\phi}{r}\frac{\partial v_\phi}{\partial z}-\frac{2}{E}\frac{\partial v_\phi}{\partial z}=\frac{\partial^2(w)}{\partial z^2}+\frac{\partial^2(w)}{\partial r^2}+\frac{1}{r}\frac{\partial w}{\partial r}-\frac{w}{r^2}+N(\boldsymbol{\nabla}\times\boldsymbol{f})_\phi,$$

$$\frac{\partial^2\psi}{\partial z^2}+\frac{\partial^2\psi}{\partial r^2}-\frac{1}{r}\frac{\partial\psi}{\partial r}=-rw,$$

$$v_z\frac{\partial\Omega}{\partial z}+v_r\frac{\partial\Omega}{\partial r}+2v_r\frac{\Omega}{r}+\frac{2}{rE}v_r=\frac{\partial^2\Omega}{\partial z^2}+\frac{\partial^2\Omega}{\partial r^2}+\frac{3}{r}\frac{\partial\Omega}{\partial r}, \tag{7}$$

where $\Omega(r,z)=v_\phi/r$. The free-surface problem is addressed using the mapping $r=\xi$, $z=(1+\eta)h(\xi)/2$, thus transferring the computational domain $0<r<1$, $0<z<h(r)$ into a rectangular domain $0<\xi<1$, $-1<\eta<1$. For more details we refer to [13].

The Navier-Stokes equation are solved by a spectral collocation code. We express the stream function, vorticity, and angular velocity via base functions constructed from orthogonal Chebyshev polynomials $T_n(x)$ to meet already a part of the boundary conditions; for further details we again refer to [13]. Only even Chebyshev polynomials are used in the ξ direction [4,20]. The Chebyshev collocation points $\xi_i=-\cos[\pi(i+n_r)/(2n_r)]$, $i=0,\ldots,n_r$, and $\eta_k=-\cos(\pi k/n_z)$, $k=0,\ldots,n_z$, are used. Note that collocation points η_k on the symmetry axis $\xi=0$ are used, too.

The free-surface position can be found from the dynamical boundary condition [19], which in the absence of an external gas pressure is obtained as

$$p-2(e_{rr}n_r^2+e_{zz}n_z^2+2e_{rz}n_rn_z)+G(K_1+K_2)/\mathrm{Bo}=0, \tag{8}$$

where e_{ij} are the stress tensor components, $n_r=-h_\xi/\sqrt{1+h_\xi^2}$, $n_z=1/\sqrt{1+h_\xi^2}$ are components of the surface normal vector, and the Bond number is given by $\mathrm{Bo}=\rho gR_0^2/\gamma$. The curvatures K_1 and K_2 can be found from

$$K_1+K_2=\frac{h_\xi}{\xi\sqrt{1+h_\xi^2}}+\frac{h_{\xi\xi}}{(1+h_\xi^2)^{3/2}}.$$

The pressure is obtained from the Navier-Stokes equation in the following way. We multiply the steady Navier-Stokes equation (6) with a unit vector $\boldsymbol{\tau}$ tangentional to the free surface (its components are $\tau_\xi=1/\sqrt{1+h_\xi^2}$, $\tau_\eta=h_\xi/\sqrt{1+h_\xi^2}$):

$$\boldsymbol{\tau}\cdot\boldsymbol{\nabla}P=\boldsymbol{\tau}\cdot[\Delta\boldsymbol{v}+N\boldsymbol{f}-(\boldsymbol{v}\cdot\boldsymbol{\nabla})\boldsymbol{v}].$$

Integrating this expression from $\xi=0$ to ξ along the free surface yields

$$P(\xi)=P_0+\int_0^\xi\boldsymbol{\tau}\cdot[\Delta\boldsymbol{v}+N\boldsymbol{f}-(\boldsymbol{v}\cdot\boldsymbol{\nabla})\boldsymbol{v}]ds,$$

where P_0 is a reference value. In order to calculate this integral we must know the Lorentz force components, which may be easily found from the magnetic potential vector A_ϕ,

$$f_z=\frac{1}{2}\mathrm{Im}\left(A_\phi\frac{\partial A_\phi^\star}{\partial z}\right),\quad f_r=\frac{1}{2}\mathrm{Im}\left(A_\phi\frac{\partial A_\phi^\star}{\partial r}\right).$$

At a point where the free surface contacts the sidewall of the container ($\xi=1$, $\eta=1$) we apply an additional boundary condition related to the contact angle α_0 there, which represents an additional independent parameter of the problem:

$$h_\xi(\xi=1)=\cot(\alpha_0). \tag{9}$$

Independent of the surface deformation, the total volume of a liquid should be constant, which for a unit aspect ratio yields

$$\int_0^1 h(\xi)\xi\,d\xi=1.$$

The resulting system of nonlinear equations is solved by a Newton method, in which a simple Gauss elimination method is used for the solution of related linear equation systems. Thus, for a given free surface we find the vector potential A_ϕ, then the Lorentz force $\boldsymbol{f}$, then the fluid flow

TABLE I. Meridional Reynolds number Re and maximum angular velocity Ω_m calculated for various collocation point numbers $n_r=n_z=n$ for $N=10^7$, $E=0.1$.

n	30	36	40	44
Re	125.252	125.189	125.203	125.202
Ω_m	95.6807	95.6808	96.6800	96.6802

solution, and then a related new free-surface position. The process repeats until convergence is reached.

The meridional flow in the liquid is basically driven by the Lorentz force, the strength of which scales with the magnetic interaction parameter N. The resulting dimensionless meridional velocity $v_m=\sqrt{v_z^2+v_r^2}$ depends on the input parameter of the problem, but may be much larger than 1. We define the meridional Reynolds number as $\mathrm{Re}=\max(v_m)$. In Table I we show some results of the flow calculations for the purpose of code validation. Here the free surface is fixed to be flat, the Ekman number is $E=0.1$, the interaction parameter $N=10^7$, the frequency $\omega=2\times10^2$, the Bond number $\mathrm{Bo}=1$, the dimensionless gravity $G=3.5\times10^6$, the contact angle $\alpha=\pi/2$, and the aspect ratio is fixed to 1. We repeated the calculations with various values of collocation points $n_r=n_z=n$. Table I gives the Re values and also the maximum angular velocity $\Omega_m=\max[\Omega(\xi,\eta)]$. It is seen that so-called spectral convergence is reached. Table II shows the results for a larger Reynolds number. In this case it is necessary to use more collocation points for convergence.

D. Results for the base flow

We consider the flow of a liquid metal or a liquid metal alloy with a typical density $\rho\sim3\times10^3$ kg/m^3, electrical conductivity $\sigma\sim10^6-10^7$ S/m, kinematic viscosity $\nu\sim10^{-6}$ m^2/s, and surface tension $\gamma\sim1$ N/m in a container of $R_0\sim5-10$ mm in an external ac magnetic field with a frequency of $f_0\sim10^5$ Hz. The independent, nondimensional parameters of the problem are the ac field frequency ω, the interaction parameter N, the Ekman number of the container rotation E, the relative gravity G, the Bond number Bo, and the contact angle α_0. In our study we fix $G=3.5\times10^6$, $\mathrm{Bo}=1$, $\omega=2\times10^2$ (i.e., skin depth $\delta=0.1$), the contact angle to $\alpha_0=\pi/2$ and limit all calculations to an aspect ratio of 1 for the liquid in the container. We mainly consider variations of two control parameters of the problem, the interaction parameter N and the Ekman number E.

Figure 2 shows the stream function ψ (left) and angular velocity Ω (right) isolines at a fixed interaction parameter $N=10^7$ and various Ekman numbers $E=0.1$ (a), 1×10^{-2} (b), 1×10^{-3} (c), and 2×10^{-4}(d). In all four cases the flow consists of four toroidal eddies. The flow is vertically nonsymmetric, due to the different boundary conditions of a rigid wall at the bottom and a free surface on top. The arrows show the directions of the flow; the signs (+) and (−) indicate the direction of the related azimuthal motion. Increasing spinning (reducing E) leads to a suppression of the meridional flow. The upper boundary is almost flat at $E>1\times10^{-3}$ and only at $E<2\times10^{-4}$ does the deformation of the free surface become significant. Figure 3 shows the meridional Reynolds number Re and the maximum absolute value of the azimuthal velocity v_ϕ versus the Ekman number E for interaction parameter $N=10^7$. For large E, which corresponds to a slow rotation, the Reynolds number effectively depends only on the interaction parameter N but not on E. Increase of N results in larger Re, which corresponds to a stronger meridional flow. Reduction of E, corresponding to a faster-spinning container, results in a suppression of the meridional flow characterized by a reduced Reynolds number. Damping of the meridional flow becomes effective for $E<0.01$, where a rather strong reduction of the meridional flow takes place for further decreasing E. A deviation of the fluid rotation from the related solid body rotation, characterized by v_ϕ in the rotating frame of reference, develops as the container starts to spin. In a slowly spinning container ($E\gg1$), the azimuthal velocity is small because the Coriolis force, which is responsible for the differential rotation in the fluid, is weak in this case. In a rapidly spinning container ($E\ll1$), the azimuthal velocity decreases with increasing spinning rate in accordance with the Proudman theorem, which requires the fluid flow to be nearly uniform along the axis of a rapidly rotating fluid. Hence, the azimuthal velocity has a maximum at an intermediate Ekman number $E\sim0.001-0.01$.

TABLE II. Meridional Reynolds number Re and maximum angular velocity Ω_m calculated for various collocation point numbers $n_r=n$, $n_z=n+22$ for $N=5.209\,68\times10^7$, $E=10^2$.

n	14	22	30	38
Re	378.666	377.725	377.876	377.851
Ω_m	0.546600	0.550893	0.551141	0.550849

III. LINEAR THREE-DIMENSIONAL STABILITY ANALYSIS

A. Approach and numerical method

For the linear stability analysis, the Navier-Stokes equation (6) was linearized around the steady axisymmetric base flow and then solved by marching in time for each azimuthal wave number m separately. These linearized equations in the rotating frame of reference are

$$\frac{\partial \boldsymbol{v}}{\partial t}+(\boldsymbol{v}_0\cdot\boldsymbol{\nabla})\boldsymbol{v}+(\boldsymbol{v}\cdot\boldsymbol{\nabla})\boldsymbol{v}_0+\frac{2}{E}\boldsymbol{e}_z\times\boldsymbol{v}=-\boldsymbol{\nabla}P+\Delta\boldsymbol{v},$$

$$\boldsymbol{\nabla}\cdot\boldsymbol{v}=0, \tag{10}$$

where $\boldsymbol{v}_0$ is the base flow and $\boldsymbol{v}$ is a small three-dimensional disturbance. The axisymmetric case of $m=0$ was considered as well. We seek the solution as

$$\boldsymbol{v}=\mathbf{e}_z v_z(z,r)\cos(m\phi)+\mathbf{e}_r v_r(z,r)\cos(m\phi)+\mathbf{e}_\phi v_\phi(z,r)\sin(m\phi),$$

$$P=p(r,z)\cos(m\phi).$$

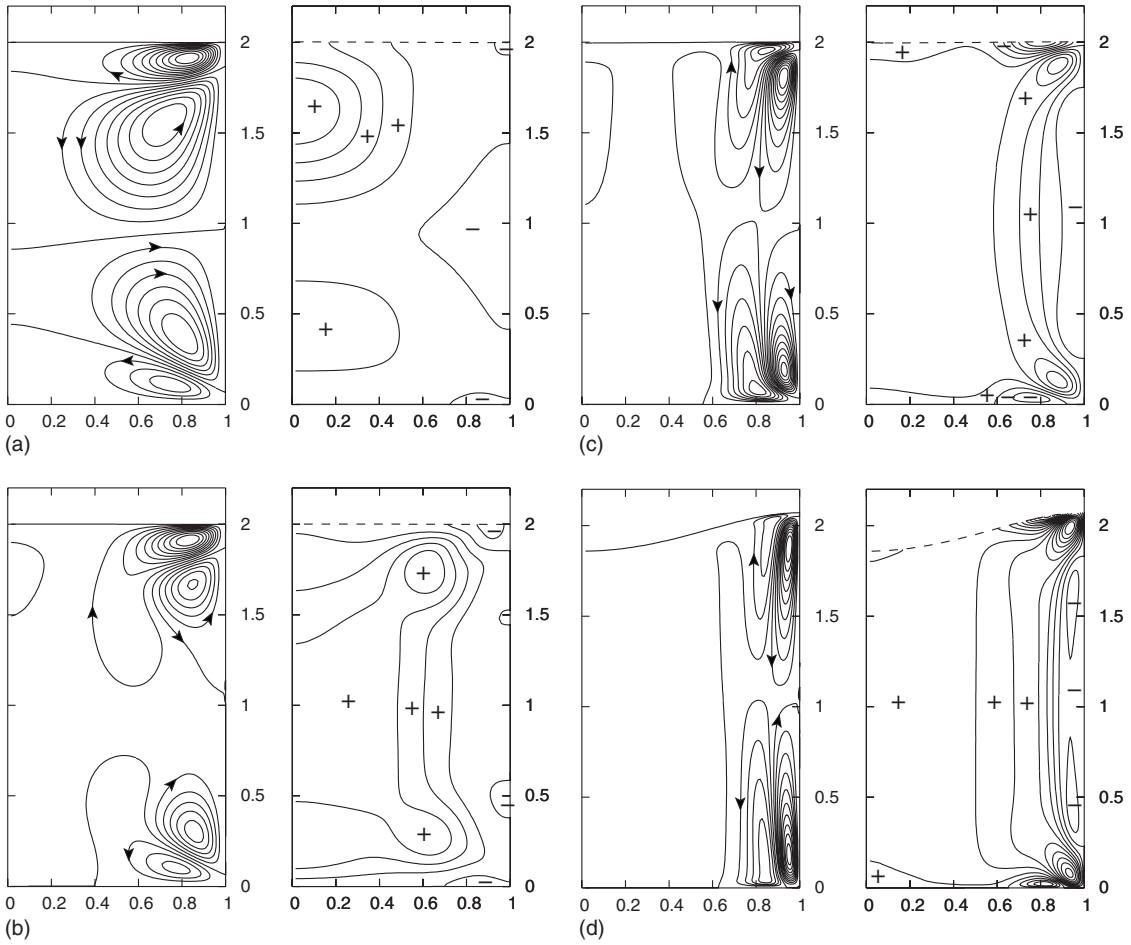

FIG. 2. Stream function ψ (on the left) and angular velocity Ω (on the right) isolines for interaction parameter $N=10^7$ and Ekman numbers $E=0.1$ (a), 1×10^{-2} (b), 1×10^{-3} (c), and 2×10^{-4} (d). The level spacings for stream function and angular velocity are 0.1 and 0.2, respectively.

which leads to the equations

$$\frac{\partial v_z}{\partial t} + K_z = -\frac{\partial p}{\partial z} + \left(\frac{\partial^2 v_z}{\partial z^2} + \frac{\partial^2 v_z}{\partial r^2} + \frac{1}{r}\frac{\partial v_z}{\partial r} - \frac{m^2 v_z}{r^2}\right),$$

$$\frac{\partial v_r}{\partial t} + K_r = -\frac{\partial p}{\partial r} + \left(\frac{\partial^2 v_r}{\partial z^2} + \frac{\partial^2 v_r}{\partial r^2} + \frac{1}{r}\frac{\partial v_r}{\partial r} - \frac{(1+m^2)v_r}{r^2} - \frac{2mv_\phi}{r^2}\right),$$

$$\frac{\partial v_\phi}{\partial t} + K_\phi = \frac{mp}{r} + \left(\frac{\partial^2 v_\phi}{\partial z^2} + \frac{\partial^2 v_\phi}{\partial r^2} + \frac{1}{r}\frac{\partial v_\phi}{\partial r} - \frac{(1+m^2)v_\phi}{r^2} - \frac{2mv_r}{r^2}\right),$$

$$\frac{\partial v_z}{\partial z} + \frac{1}{r}\frac{\partial r v_r}{\partial r} + \frac{mv_\phi}{r} = 0, \tag{11}$$

where K_z, K_r, and K_z are linearized convective terms, which are written in a rotational form [21]. It is convenient to introduce new variables $v_+=v_r+v_\phi$, $v_-=v_r-v_\phi$, since the resulting equations for v_+, v_- are decoupled [4].

The base flow calculations showed that relevant surface deformations occurred only for $E<2\times10^{-4}$, and thus only at rather high spinning rates of the cylinder. Therefore, we re-

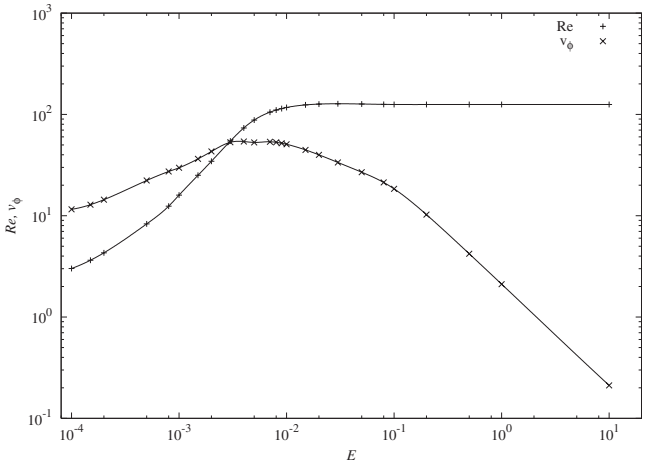

FIG. 3. Meridional Reynolds number Re versus Ekman number E for interaction parameter $N=2\times10^7$.

strict the stability analysis to the case of a flat free surface, i.e., $h(r)=2$ since the aspect ratio is fixed to unity. This leads to a significant reduction of the numerical efforts as the magnetic field calculation decouples in this case from the fluid flow calculations. As we shall see finally, the interesting stability phenomena typically occur at $E>10^{-3}$, for which the assumption of a flat free surface is certainly satisfied. In this case, the boundary conditions simplify to

$$v_z = v_r = v_\phi = 0 \quad \text{at } z=0 \text{ and at } r=1,$$

$$v_z = 0, \quad \frac{\partial v_r}{\partial z} = 0, \quad \frac{\partial v_\phi}{\partial z} = 0 \quad \text{at } z=2. \tag{12}$$

To solve Eqs. (11) we use the two-step splitting method [21]:

$$\frac{11\boldsymbol{v}^* - 18\boldsymbol{v}^n + 9\boldsymbol{v}^{n-1} - 2\boldsymbol{v}^{n-2}}{6\,dt} = -\boldsymbol{K}^* + \Delta\boldsymbol{v}^*, \tag{13}$$

$$\Delta\Phi = \frac{11}{6\,dt}\nabla\cdot\boldsymbol{v}^*, \tag{14}$$

$$\mathbf{v}^{n+1} = \mathbf{v}^* - \frac{6\,dt}{11}\nabla\Phi, \tag{15}$$

where Φ is a projection function, dt is a time increment, and the upper index n denotes the time level (time$=n\,dt$). The convective term $\boldsymbol{K}^*$ is found by a third-order Adams-Bashford extrapolation method $\boldsymbol{K}^*=3(\boldsymbol{K}^n-\boldsymbol{K}^{n-1})+\boldsymbol{K}^{n-2}$, and the boundary conditions for the projection function Φ are $\frac{\partial\Phi}{\partial\boldsymbol{n}}=0$, where $\boldsymbol{n}$ is a unit vector orthogonal to the boundary. There is a well-known boundary condition problem [21] for the intermediate velocity $\boldsymbol{v}^*$. As on the upper surface the boundary conditions (12) are of Neumann type, the simple shift of the velocity using the old value of the projection function Φ cannot be applied here [21]. To avoid this problem we apply the matrix influence technique. On each time step we solve Eq. (13) at first with the boundary condition $\boldsymbol{v}^*=\mathbf{0}$ on the boundary of the computational domain. After that we find the projection function Φ from (14) and determine the preliminary value of $\tilde{\boldsymbol{v}}^{n+1}$ from (15). In the preliminary part of the calculations we additionally solve the system of equations

$$\frac{11\boldsymbol{u}_{ii}^*}{6dt} - \Delta\mathbf{u}_{ii}^* = \mathbf{0}, \tag{16}$$

$$\Delta\Phi_{ii} = \frac{11}{6\,dt}\nabla\cdot u_{ii}^*, \tag{17}$$

$$\boldsymbol{u}_{ii}^{n+1} = \boldsymbol{u}_{ii}^* - \frac{6\,dt}{11}\nabla\Phi_{ii}, \tag{18}$$

where special boundary conditions are applied for the u_{ii}^*. In all boundary collocation points the normal component of the velocity (u_z^* at bottom and top boundaries and u_r^* at $r=1$) is equal to zero. The tangential components are also zero in all boundary collocation points except one point, where one of the tangential velocity components is equal to 1. The full number of boundary collocation points is $n_b=2(n_r-1)+n_z-1$; thus the system of equations (16)–(18) is solved $2n_b$ times. Then the velocity $\boldsymbol{v}^{n+1}$ can be improved:

$$\boldsymbol{v}^{n+1} = \tilde{\boldsymbol{v}}^{n+1} + \sum_{ii=1}^{2n_b} c_{ii}\boldsymbol{u}_{ii}^{n+1},$$

where the unknown coefficients c_{ii} are found to satisfy the velocity boundary conditions (12). In this part of our study, the Poisson and Helmholtz equations are solved by a pseudospectral method directly at the collocation points using the eigenfunction diagonalization technique [22].

In order to test the numerics we chose some steady two-dimensional flow,

$$v_{0,z}(z,r) = (6r^4 - 8r^2 + 2)(2z^2 - 5z/3 + z^4/3),$$

$$v_{0,r}(z,r) = (-r^5 + 2r^3 - r)(4z - 5z^2 + 4z^3/3),$$

$$v_{0,\phi}(z,r) = (r - r^3)(z - z^2/4),$$

and a time-periodic three-dimensional flow,

$$v_z(z,r) = [-4(m+1)r^m + 24(m+2)r^{m+2} - 36(m+3)r^{m+4} + 16(m+4)r^{m+6}]g(s)\sin(\omega t),$$

$$v_r(z,r) = [(m+2)r^{m+1} - 3(m+4)r^{m+3} + 3(m+6)r^{m+5} - (m+8)r^{m+7}]f(s)\sin(\omega t),$$

$$v_\phi(z,r) = -m(r^{m+1} - 3r^{m+3} + 3r^{m+5} - r^{m+7})f(s)\sin(\omega t),$$

$$p(z,r) = (r^{m+2} - r^{m+4})(z^2 - 2z)/(m+2)\sin(\omega t), \tag{19}$$

with $g(s)=-s^5+s^4+2s^3-2s^2-s+1$, $f(s)=-5s^4+4s^3+6s^2-4s-1$, and $s=z-1$. Those flow fields are solutions of the steady two-dimensional and the nonsteady three-dimensional Navier-Stokes equations, respectively, when some additional artificial forces are added. These force components can easily be found analytically. The artificial force components are then included into the numerical scheme, and the equations are integrated up to the time $t=3$. In the test case we used $E=100$, $m=5$, $\omega=\pi/2$. The numerical solution contains errors due to both the space and the time approximations. First we obtained the solution with time increment $dt=5\times10^{-3}$ and various collocation point numbers $n_r=n_z$. The numerical solutions were compared to the exact test solution (19). Figure 4 shows that there is a so-called spectral convergence when the number of collocation points increases. In a second step we fixed the collocation points to $n_r=n_z=50$ and repeated the calculations with various time increments dt. Figure 5 shows that we obtained a third-order convergence rate of the temporal approximation. In this test case all velocities were small, and it was possible to provide calculations in a broad range of time increments dt. In the real case of the considered spinning cylinder, the base flow velocity is typically much larger. This and also the small values of the Ekman number E lead to the usual numerical stability restriction for the time increment dt. For those reasons we used $dt\sim10^{-5}$.

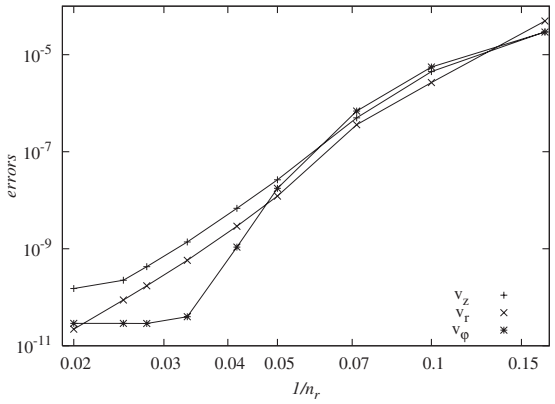

FIG. 4. Errors of the velocity components in the test case versus the inverse number of collocation points $1/n_r$ ($n_z=n_r$, $dt=2\times10^{-3}$).

B. Stability results

We calculated first the basic axisymmetric flow with a fixed free-surface position for given values of the interaction parameter N and Ekman number E. Then we added some initial disturbances to the three-dimensional velocity components and marched in time the linearized Navier-Stokes equations. After some time the most unstable mode began to dominate in the solution. Then we found the growth rate λ_r and the frequency λ_i numerically, calculating the full kinetic energy growth of the linear three-dimensional solution and monitoring the time dependence of the velocity at some collocation points as well. We have also used the method of Goldhirsch *et al.* [23], which leads to a significant reduction of the calculation times. Usually we found by this method four or six eigenvalues.

After that we repeated the two-dimensional base flow calculations with another value of the interaction parameter N. The critical value N_c corresponds to the growth rate $\lambda_r^{cr}=0$. We repeated the stability analysis for various azimuthal wave numbers m and found that in the case of large Ekman numbers $E\gg1$ the flow is most unstable for $m=3$. The instability is of oscillatory type. At an Ekman number of $E=100$ the critical meridional Reynolds number is Re=377.88 and the frequency $\lambda_i^{cr}=126.8$, whereas the critical interaction parameter is $N_c=5.21\times10^7$. Figure 6 shows the critical Reynolds number versus the Ekman number. When we reduce the Ekman number from $E=100$ to a smaller value, the critical meridional Reynolds number is reduced as well. It means that slow container spinning increases the instability of the base flow. At an Ekman number of $E=4.614\times10^{-2}$, the most unstable azimuthal wave number is changed from $m=3$ to 5 and the instability is changed from oscillatory type to a steady one. For smaller Ekman numbers the most unstable azimuthal wave number increases again to $m=6$ at $E=4.16\times10^{-3}$, to $m=7$ at $E=2.61\times10^{-3}$, etc. Eventually, at small Ekman numbers $E=2.1\times10^{-4}$ the most unstable wave number is $m=16$. Our approximation of the free surface as a flat one is not valid at very small Ekman numbers, as was shown in the two-dimensional analysis. Therefore, we did not consider Ekman numbers $E<2\times10^{-4}$ in this stability analysis. Except for a narrow interval $1.935\times10^{-2}<E<2.376\times10^{-2}$ where the instability is of oscillatory type again, for all other values of $E<4.614\times10^{-2}$ the instability is of steady type. The lowest critical value of the meridional Reynolds number is Re=30.77 at $E=9.15\times10^{-4}$, at smaller Ekman numbers it slowly increases. At the smallest considered

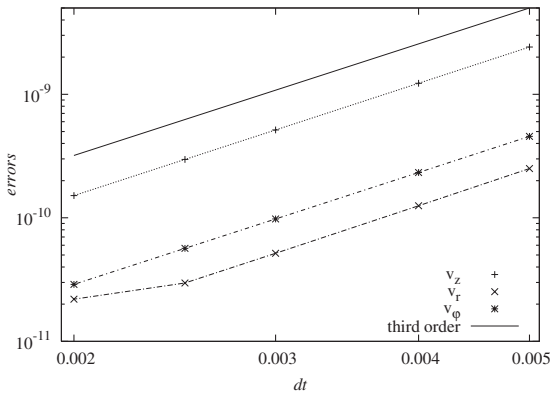

FIG. 5. Errors of the velocity components in the test case versus the time increment dt ($n_r=n_z=50$).

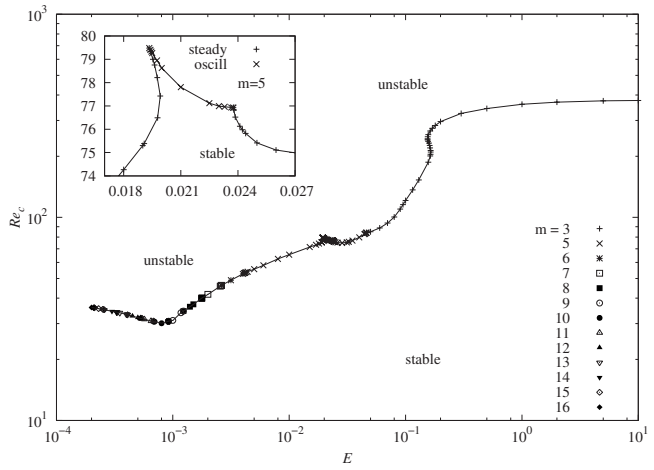

FIG. 6. Critical value of the meridional Reynolds number Re_c versus Ekman number E. The inset shows the neutral curve near the Ekman number $E=0.22$.

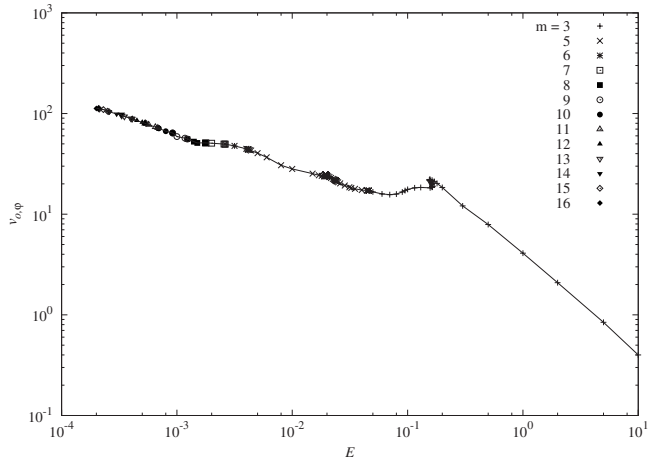

FIG. 7. Maximum value of the base azimuthal velocity v_ϕ versus Ekman number E.

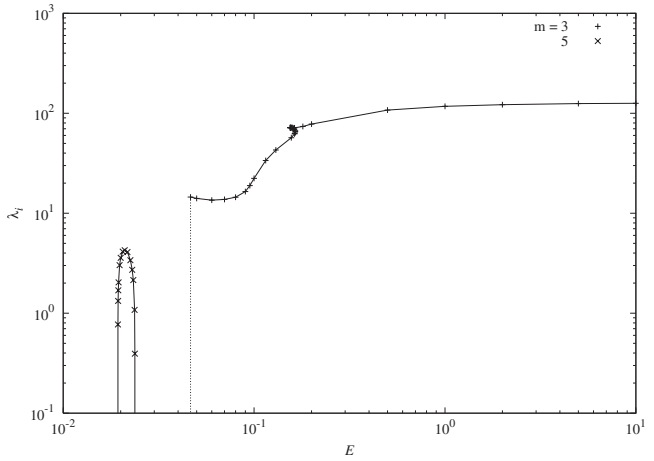

FIG. 8. Neutral frequency λ_i^{cr} versus Ekman number E.

value of $E=2\times10^{-4}$ the meridional Reynolds number is Re=36. Figure 7 shows the maximum of the azimuthal velocity $v_{0,\phi}$ versus the Ekman number E at values of the interaction parameter N that correspond to the neutral curve in Fig. 6. Figure 8 shows the frequency λ_i^{cr} of the most unstable mode versus the Ekman number. Note that there are nonmonotonic parts of the neutral stability curve in Fig. 6 in the intervals of Ekman numbers $0.15<E<0.17$ and $0.018<E<0.027$; the latter interval is zoomed in the inset of Fig. 6. Corresponding nonmonotonic intervals are contained in Fig. 7. The transitions from one most unstable azimuthal wave number value to another one lead to the kinks in the neutral curves. The inset in Fig. 6 shows that the steady instability changes to an oscillatory one with the same azimuthal wave number $m=5$ at $E=2.38\times10^{-2}$ and again to a steady instability at the smaller Ekman number $E=1.93\times10^{-2}$. The frequency changes smoothly from zero to a finite value and again to zero in this range of Ekman numbers, as one can see in Fig. 8.

If we redefine the nondimensional time as the ratio of the cylinder radius to the maximum of the meridional velocity, i.e., $t_0=R_0/\mathrm{Re}$, then the nondimensional frequency of the disturbed flow becomes $f=\lambda_i^{\mathrm{cr}}/\mathrm{Re}=0.3356$ for $E=100$ at neutral stability. It is interesting to note that the flow inside a spherical droplet [24] in an external uniform alternating magnetic field is also unstable to three-dimensional disturbances with $m=3$, and the corresponding frequency has the same order of magnitude.

To investigate the energy transfer from the base to the disturbed flow we analyze the kinetic energy of the three-dimensional (3D) disturbance by multiplying the linearized Navier-Stokes equation with the velocity vector $\boldsymbol{v}$. Azimuthal integration yields

$$S_{3\mathrm{D}}(z,r) = -\frac{1}{2\pi}\int_0^{2\pi} \boldsymbol{v}\cdot\boldsymbol{K}\, d\phi,$$

$$E_{3\mathrm{D}}(z,r) = \frac{1}{4\pi}\int_0^{2\pi} \boldsymbol{v}\cdot\boldsymbol{v}\, d\phi,$$

where $S_{3\mathrm{D}}(z,r)$ is the source density of the disturbed flow kinetic energy density $E_{3\mathrm{D}}(z,r)$. Figure 9 shows the stream-function isolines, Fig. 9(a), the base flow angular velocity isolines, Fig. 9(b), the source $S_{3\mathrm{D}}(z,r)$ isolines, Fig. 9(c), and the energy density $E_{3\mathrm{D}}(z,r)$ isolines, Fig. 9(d), for the values of $E=10^2$, Re=377.88 on the neutral stability curve. The maximum of the energy transfer from the base to the disturbed flow $S_{3\mathrm{D}}(z,r)$ and the maximum of the disturbed flow kinetic energy density $E_{3\mathrm{D}}(z,r)$ are both located in a region where the flow in the second toroidal vortex (looking from above) is directed radially outward. There is no evident correlation between the structure of the angular velocity and the kinetic energy density $E_{3\mathrm{D}}$ isolines.

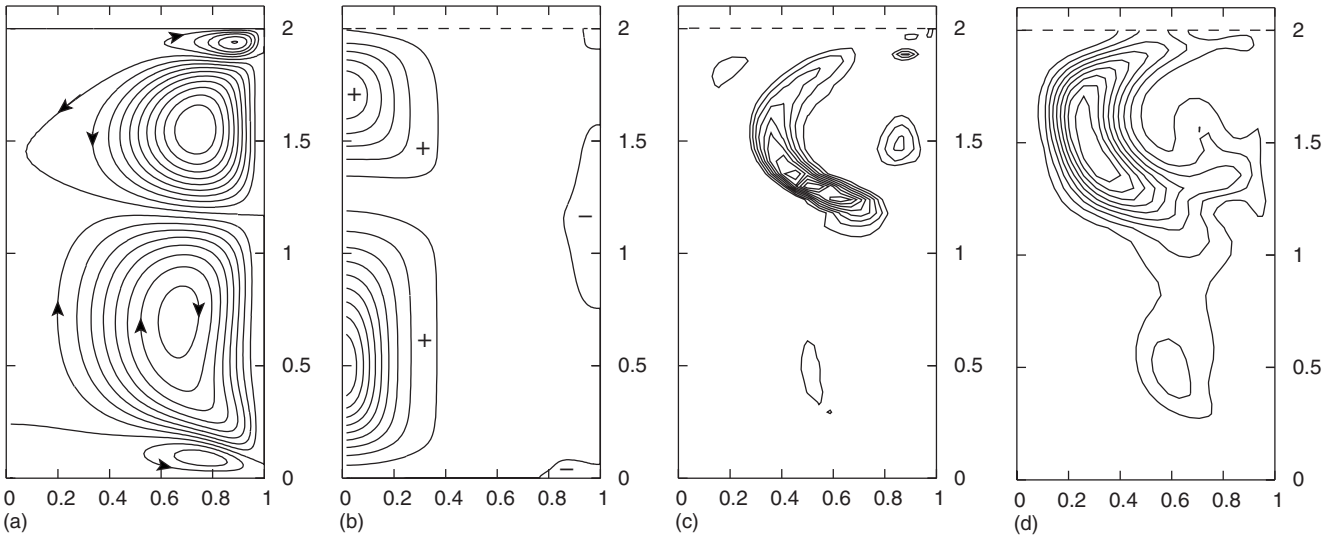

FIG. 9. Pattern of the meridional base flow (a), the angular base flow velocity (b), the three-dimensional kinetic energy source $S_{3\mathrm{D}}(z,r)$ (c), and the three-dimensional kinetic energy density $E_{3\mathrm{D}}(z,r)$ (d) for the neutral curve point $E=10^2$, Re=377.88. The level spacing is 0.1 normalized to each maximum value.

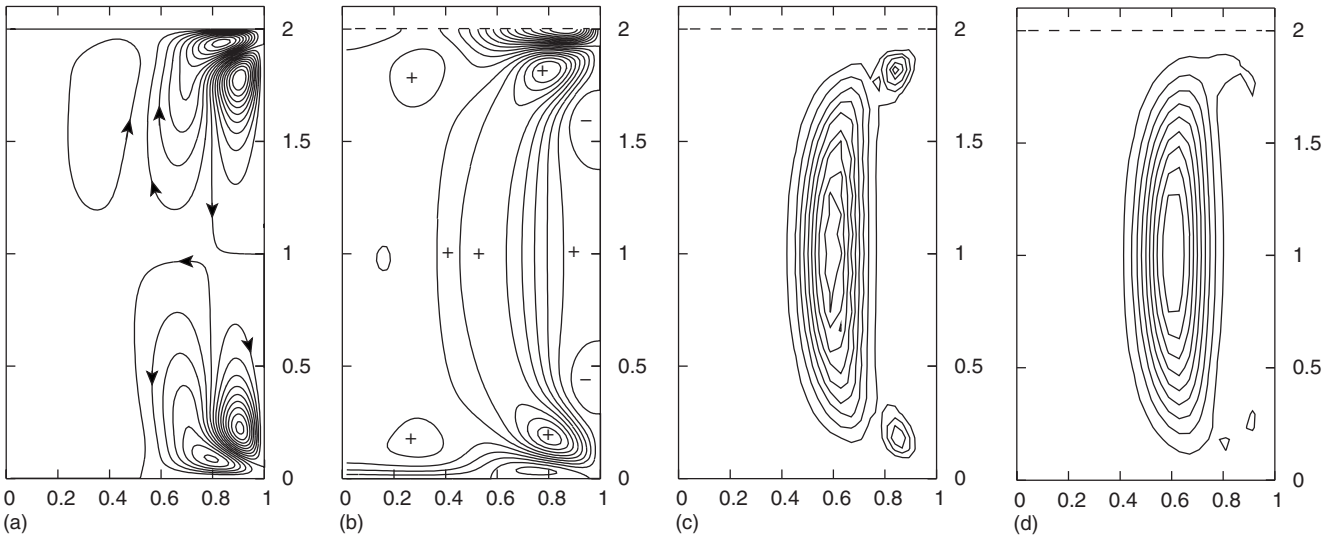

FIG. 10. Pattern of the meridional base flow (a), the angular base flow velocity (b), the three-dimensional kinetic energy source $S_{3D}(z,r)$ (c), and the three-dimensional kinetic energy density $E_{3D}(z,r)$ (d) for the neutral curve point $E=2.61\times10^{-3}$, Re=46.237. The level spacing is 0.1 normalized to each maximum value.

Figure 10 shows the same results as Fig. 9, but now for the much lower Ekman number of $E=2.61\times10^{-3}$ which on the neutral stability curve corresponds to a meridional Reynolds number of Re=46.237. The stream-function isolines in Fig. 10(a) show an additional toroidal vortex which is driven by the main upper vortex. There is no evident correlation here between the structure of the meridional flow and the disturbed energy density $E_{3D}(z,r)$ or the kinetic energy source density $S_{3D}(z,r)$. But there is an evident similarity between the base angular velocity structure and the structure of the three-dimensional flow. Figure 11 shows the azimuthal base flow profile $v_{0,\phi}(r)$ at $z=1$. The local maximum of $v_{0,\phi}(r)$ is located in good approximation in the region where the values of S_{3D} and E_{3D} have their maxima. We did the following numerical experiment: artificially we deleted some of the base velocity components and for this new base flow we repeated the stability analysis for the same control parameters $E=2.61\times10^{-3}$, $N=9.92\times10^{6}$. If the azimuthal base flow velocity components are deleted, the growth rate is reduced from zero to $\lambda_r=-152.7$, thus the base flow is stable. If, instead, the meridional velocity components are deleted from the same base flow, then the growth rate is increased to $\lambda_r=2.627$. Hence, in the absence of meridional velocity components the flow became even more unstable.

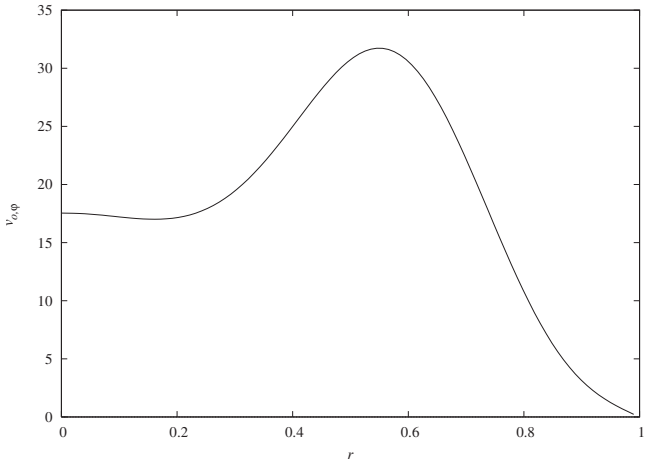

FIG. 11. Azimuthal base velocity profile $v_{0,\phi}(r,z=1)$ for the neutral curve point $E=2.61\times10^{-3}$, Re=46.237.

Actually, in the absence of any Lorentz force driving of the meridional flow there is no secondary azimuthal flow and the fluid is spinning like a solid body together with the container. As we can see from the considered examples in the case of large Ekman numbers $E\gg1$, the three-dimensional instability of the base flow is related to the instability of the base meridional flow, whereas in the case of small Ekman numbers $E\ll1$ the instability is related to the secondary azimuthal base flow. In a range of intermediate Ekman numbers both base flow parts are of relevance. As a result, the neutral stability curve in Fig. 6 has the S-shape fragment at $E\approx0.15$.

The neutral stability curve in the case of a spinning droplet [10] is nonmonotonic, too. At intermediate Ekman numbers of $E\sim10^{-2}$ the flow in a spinning droplet is more unstable than in the absence of spinning. For very small Ekman numbers the instability occurs at much larger values of the interaction parameter N (Fig. 5 of [10]) and the corresponding meridional Reynolds numbers are larger than in the nonspinning case (Fig. 1 of [10]). In the present study at $E=2\times10^{-4}$, the neutral stability value of the meridional Reynolds number is still smaller than in the nonspinning case. Figure 12 shows the critical value of the interaction parameter N_c at which the first unstable mode appears versus the Ekman number E. In the Ekman number range of $3.5\times10^{-4}<E<0.2$ the container spinning leads to a significant destabilizing effect. A similar but not so strong effect was found in the spinning droplet case [10]. Only a very strong container rotation leads to a stabilization at which the three-dimensional base flow instability occurs at larger values of the interaction parameter N_c than in the nonspinning case.

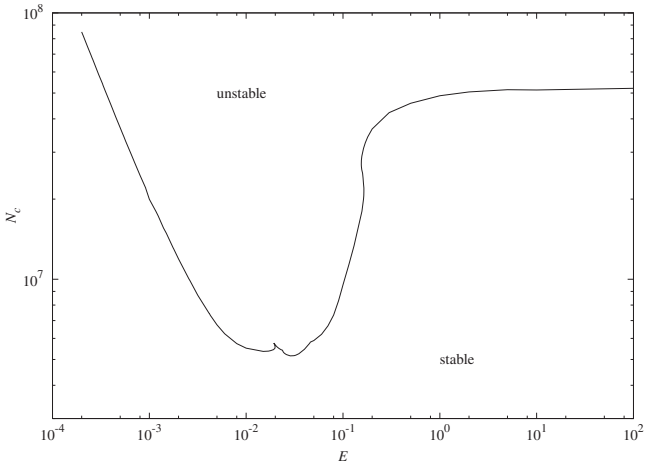

FIG. 12. Critical interaction parameter N_c at which the first unstable mode appears versus Ekman number E.

IV. CONCLUSIONS

Liquid metal flow driven by an alternating magnetic field in a cylindrical container is studied numerically. The shape of the upper free surface was found simultaneously with the flow by a Newton method. It is found that in all considered parameter ranges the flow consists of four main toroidal eddies, which is caused by the nonuniformity of the magnetic field near the edges of the liquid volume. The electromagnetic interaction parameter N controls the intensity of the flow. The additional container spinning leads to a deformation of the flow structure. At Ekman numbers $E<1\times10^{-2}$ the meridional flow is significantly reduced. The secondary azimuthal flow has its maximum in the Ekman number range of $E\sim10^{-3}-10^{-2}$; at smaller Ekman numbers the azimuthal flow is suppressed, too.

The three-dimensional stability analysis of the flow showed that the spinning leads mainly to a destabilization of the base flow, which becomes significant for $E<0.2$. Only at very small Ekman numbers is the flow in the spinning container more stable than in the nonspinning case. The instability at large Ekman numbers is of oscillatory type and the most unstable azimuthal wave number is $m=3$. At smaller Ekman numbers the most unstable azimuthal wave number increased to $m=5$, 6, etc., reaching $m=16$ at $E=2.1\times10^{-4}$. Except in a narrow Ekman number range around $E\approx2\times10^{-2}$, where the instability is of oscillatory type, at all other values of Ekman numbers $E<4.614\times10^{-2}$ the instability is of steady type.

This steady nonaxisymmetric bifurcation which breaks the SO(2) symmetry of the base flow may look puzzling. Note, however, that there are several examples in literature with a similar symmetry breaking by a steady bifurcation. It has been found, e.g., for the flow past a sphere [25,26], where the first unstable mode is nonaxisymmetric with wave number $m=1$, or for the flow in a cylindrical container driven by a traveling magnetic field [27,28]. In the latter case a steady bifurcation occurs as the first instability mode if the aspect ratio of the cylinder exceeds a value of about 1.2. In this case, for certain parameter values, the instability changes from an oscillatory to a steady mode with the same azimuthal wave number (Fig. 7 of [28]), a behavior similar to the switch between modes as shown in Fig. 6 of the present paper.

As mentioned in Sec. III A, we restricted the stability analysis to the case of a flat free surface of the base flow in order to limit the present analysis to the simplest case for the essential stability relations involving just the Ekman number E and the electromagnetic interaction parameter N. As it turned out, the most interesting stability phenomena indeed occur at $E>10^{-3}$, for which the assumed flat surface is certainly a good approximation. Any deviation from the flat free surface, either due to the container rotation or due to another value of the contact angle α_0, leads to a much stronger coupling between the base flow, the resulting Lorentz force distribution, and the stability analysis, which, in particular, no longer allows the direct application of the efficient pseudospectral solver for the flow problem. The nonflat free-surface case requires consideration of the three additional independent parameters (G,Bo,α_0), which is beyond the scope of the present paper and is left for a subsequent analysis.

ACKNOWLEDGMENTS

This work has been supported by Deutsche Forschungsgemeinschaft under Grant No. HE 2955/2-3 and in the frame of the Collaborative Research Center SFB 609.

[1] J. M. Lopez, F. Marques, A. H. Hirsa, and R. Miraghaie, J. Fluid Mech. **502**, 99 (2004).
[2] A. Yu. Gelfgat, P. Z. Bar-Yoseph, and A. Solan, J. Fluid Mech. **438**, 363 (2001).
[3] Yu. Gelfgat, J. Priede, and M. Z. Sorkin, in *Proceedings of the International Conference on Energy Transfer in MHD Flows, Cadarache, France*, edited by A. Alemany, G. Marbach, and Ph. Marty (Plenum, New York, 1991), p. 181.
[4] I. Grants and G. Gerbeth, J. Fluid Mech. **431**, 407 (2001).
[5] I. Grants and G. Gerbeth, J. Fluid Mech. **463**, 229 (2002).
[6] A. Pedchenko and I. Grants, Phys. Fluids **17**, 104102 (2005).
[7] N. El-Kaddah and J. Szekely, J. Fluid Mech. **133**, 37 (1983).
[8] A. Bojarevics, V. Bojarevics, Yu. Gelfgat, and K. Pericleous, Magnetohydrodynamics (N.Y.) **35**, 205 (1999).
[9] E. Baake, A. Umbrashko, and A. Jakovics, Steel Res. Int. **78**, 413 (2007).
[10] V. Shatrov, J. Priede, and G. Gerbeth, Phys. Fluids **19**, 078106 (2007).
[11] O. Filip, R. Hermann, G. Gerbeth, J. Priede, and K. Biswas, Mater. Sci. Eng., A **413-414**, 302 (2005).
[12] K. Biswas, R. Hermann, J. Das, J. Priede, G. Gerbeth, and J. Acker, Scr. Mater. **55**, 1143 (2006).

[13] V. Shatrov, G. Gerbeth, and R. Hermann, J. Fluid Eng. (in press).
[14] J. Priede and G. Gerbeth, IEEE Trans. Magn. **42**, 301 (2006).
[15] A. J. Mestel, J. Fluid Mech. **117**, 27 (1982).
[16] I. S. Gradshteyn and I. M. Ryzhik, *Tables of Integrals, Series and Products* (Academic Press, New York, 2000).
[17] J. Meixner, IEEE Trans. Antennas Propag. **20**, 442 (1972).
[18] V. I. Yakovlev, J. Appl. Mech. Tech. Phys. **37**, 459 (1996).
[19] G. K. Batchelor, *An Introduction to Fluid Dynamics* (Cambridge University Press, Cambridge, UK, 1967).
[20] L. S. Tuckerman, J. Comput. Phys. **80**, 403 (1989).
[21] C. Canuto, M. Y. Hussaini, A. Quarteroni, and T. A. Zang, *Spectral Method in Fluids Mechanics* (Springer, New York, 1987).
[22] K. Liffman, J. Comput. Phys. **128**, 254 (1996).
[23] I. Goldhirsch, S. A. Orszag, and B. K. Maulik, J. Sci. Comput. **2**, 33 (1987).
[24] V. Shatrov, J. Priede, and G. Gerbeth, Phys. Fluids **15**, 668 (2003).
[25] R. Natarajan and A. Acrivos, J. Fluid Mech. **254**, 323 (1993).
[26] A. G. Tomboulides and S. A. Orszag, J. Fluid Mech. **416**, 45 (2000).
[27] I. Grants and G. Gerbeth, J. Cryst. Growth **269**, 630 (2004).
[28] A. Gelfgat, J. Cryst. Growth **279**, 276 (2005).